ELSEVIER

Journal of Nuclear Materials 301 (2002) 129–141

journal of nuclear materials

www.elsevier.com/locate/jnucmat

Disorder-induced melting in nickel: implication to intergranular sulfur embrittlement

J.K. Heuer [a,b,*], P.R. Okamoto [a], N.Q. Lam [a], J.F. Stubbins [b]

[a] *Materials Science Division, Argonne National Laboratory, Argonne, IL 60439, USA*

[b] *Department of Nuclear, Plasma, and Radiological Engineering, University of Illinois at Urbana–Champaign, Urbana, IL 61801, USA*

Received 29 January 2001; accepted 28 November 2001

Abstract

Why and how sulfur segregation leads to intergranular embrittlement of nickel has been investigated by a combination of Auger electron spectroscopy, slow-strain-rate tensile tests, ion-implantation, and Rutherford backscattering spectrometry studies. Grain-boundary sulfur concentrations in dilute Ni–S alloys were systematically varied by time-controlled annealing of specimens at 625 °C. The critical sulfur concentration for 50% intergranular fracture of 15.5 ± 3.4 at.% S was found to be, within experimental error, equal to the critical implant concentration of 14.2 ± 3.3 at.% S required to induce 50% amorphization of single-crystal nickel during S^+ implantation at liquid nitrogen temperature. This suggests that segregation-induced intergranular embrittlement, like implantation-induced amorphization, may be a disorder-induced melting process, albeit one occurring locally at grain boundaries. In addition, a kinetic model for segregation-induced embrittlement based on Poisson statistics is introduced, and the synergistic effects of hydrogen–sulfur co-segregation on embrittlement are discussed.

1. Introduction

Despite a long and continuing effort to understand sulfur-induced intergranular embrittlement of nickel, the physics and chemistry underlying the phenomenon are still not well understood. Auger-electron-spectroscopy (AES) studies together with various tensile tests [1–5] show that the embrittlement is clearly associated with sulfur segregation to grain boundaries and that the transition from ductile to brittle behavior requires a critical intergranular concentration of sulfur. However, why and how sulfur weakens the grain boundaries and the significance of a critical intergranular sulfur concentration remain unclear. One widely accepted hypothesis assumes that embrittlement arises from sulfur-induced changes in the electronic structure that lead to weakening of the metal–metal bonds in the grain boundary [6,7]. This hypothesis, however, does not directly explain the need for a critical sulfur concentration, nor does it explain the well-known synergistic effects of hydrogen in reducing the critical sulfur concentration required for embrittlement to occur [4,5,8].

An alternate approach to the grain-boundary embrittlement problem that leads naturally to a critical solute concentration for intergranular fracture was recently proposed [9]. This new approach, based on disorder-induced melting concepts, is suggested by striking similarities in both the structure and the chemistry of solute-segregated grain boundaries and metallic glasses. Structurally, the atomic configuration of high-energy grain boundaries can be described in terms of the packing of several different types of polyhedra [10]; such packing schemes are very similar to those used to characterize the atomic disorder in metallic glasses [11]. Chemically, metal–metalloid glasses typically contain about 15–20 at.% metalloid; these concentrations are very similar to those found at metalloid-segregated grain boundaries in corresponding dilute alloys. Moreover, these critical

* Corresponding author.
E-mail address: heuer@telerama.com (J.K. Heuer).

0022-3115/02/$ - see front matter
PII: S0022-3115(02)00707-9

metalloid concentrations are also in the same range required to amorphize metallic single crystals during metalloid implantation at low temperatures [12]. Because ion-implantation-induced amorphization is a disorder-induced melting process [12], the analogy between solute-segregated grain boundaries and metallic glasses suggests the intriguing possibility that the thermodynamics and kinetics of segregation-induced intergranular fracture may be similar to those governing implantation-induced amorphization of metals. Carrying this analogy even further, it is natural to ask whether current kinetic models of ion-implantation-induced amorphization can be applied to segregation-induced intergranular fracture. These questions, recently explored in a preliminary study of sulfur-induced embrittlement of nickel [9], are examined in detail in the present paper.

The thermodynamic basis for regarding segregation-induced grain-boundary fracture as a disorder-induced melting process is illustrated in Fig. 1 [12,13], which shows the free-energy curves of a perfect crystal, two imperfect defective crystals, and the liquid phase. The defective crystals may represent any semi-crystalline region such as those found in ion-implanted single crystals or solute-segregated grain boundaries. Also shown are the ideal glass [14] that has the same entropy as a perfect crystal and two unrelaxed glasses associated with cooling rates such that their glass transition temperatures obey the relationship $T_{g1} > T_{g2} > T_K$, where T_K is the ideal glass transition temperature. Fig. 1 implies that melting can occur in two fundamentally different ways: ordinary melting and disorder-induced melting. Ordinary melting occurs when a crystal is heated at constant pressure to its thermodynamic melting temperature T_m^o, at which point its free energy equals that of the liquid. Disorder-induced melting, on the other hand, occurs at a fixed temperature $T_m^{def} < T_m^o$ by introducing static atomic disorder such that the free energy of the resulting defective crystal is raised directly to the level of the supercooled liquid. This can be regarded as a non-equilibrium melting process which at sufficiently low temperatures leads to glass formation [12]. As the free energy of the defective crystal increases with the introduction of atomic disorder, its melting temperature T_m^{def} decreases and approaches T_K. At this point, melting becomes a second-order phase transformation, and introducing any further disorder would simply result in a thermodynamic driving force for a phase transformation. If the damage process occurs at temperatures where thermally activated diffusion is negligible ($T < T_K$), the resulting phase will be a glass. If the damage process occurs at higher temperatures ($T > T_K$), the resulting phase will be a supercooled liquid. Hence, the thermodynamic criterion for disorder-induced glass formation becomes $T_m^{def} = T_K$.

The decrease in melting temperature with increasing static atomic disorder represents a generalized polymorphous melting curve for defective crystals [12]. For the case where static atomic displacements are produced solely by misfitting solute atoms, the composition dependence of T_m^{def} becomes equivalent to the conventional T_0 curve. This curve is shown superimposed on the equilibrium phase diagram in Fig. 2 for the Ni–S system. The dotted T_0 curve represents the locus of points where the free energies of the crystalline solid solution and the binary liquid of the same composition are equal. Since the T_0 curve drops rapidly to 0 K as the sulfur concentration approaches 18 at.% S, this indicates that there is a thermodynamic driving force for the Ni–18 at.% S alloy to transform to a glass at temperatures below T_K. Hence, the critical solute concentration for disorder-

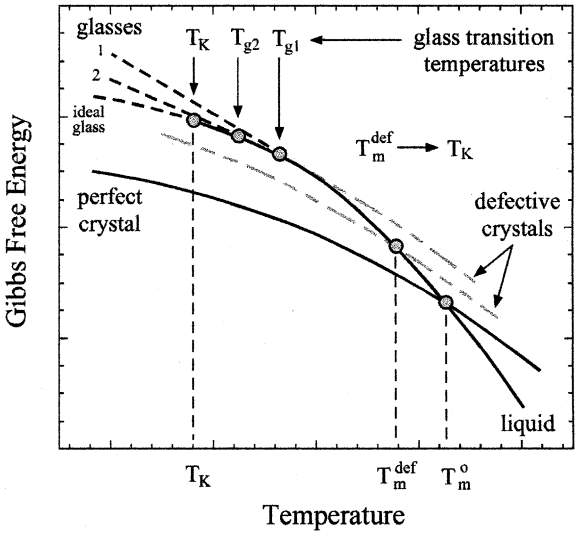

Fig. 1. Thermodynamic basis for disorder-induced melting concept.

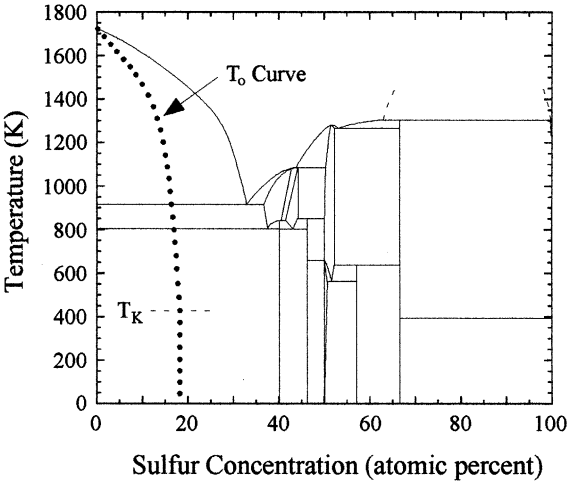

Fig. 2. Estimated polymorphous melting T_0 curve superimposed on binary Ni–S phase diagram.

induced melting below T_K is approximately 18 at.% S. This is only an estimation, however, because the T_0 curve in the figure is approximated as the midpoint between the solidus and liquidus curves. While a more accurate method to determine this critical concentration is by first-principles thermodynamic calculation, insufficient data on the properties of the supercooled liquid state exist to make this possible. However, this concentration can be measured experimentally by ion implantation. Ion implantation provides a controllable means of introducing solute atoms into a monatomic metal matrix, and the critical solute concentration necessary for disorder-induced melting can be determined by monitoring the formation of the amorphous phase during low-temperature implantation. While ion implantation also introduces disorder in the form of point defects and defect clusters, the atomic misfit between unlike atoms appears to be the primary source of stable atomic disorder. This is illustrated by the absence of amorphization during self-ion implantation [15]. In addition, the relation between the critical solute concentration predicted by the polymorphous melting curve and that required for solid-state amorphization has been pointed out in several binary systems [12].

In the present study, the hypothesis that intergranular embrittlement results from localized disorder-induced melting at solute-segregated grain boundaries is investigated. Direct measurements of the critical sulfur concentration at grain boundaries in nickel necessary to induce 50% intergranular fracture are compared to the critical sulfur concentration necessary to induce 50% amorphization of single-crystal nickel during S^+ implantation at liquid nitrogen temperatures. As will be shown, the critical concentrations are equal within experimental error, which provides strong support for the melting hypothesis for intergranular fracture.

2. Experimental procedure

2.1. Segregation-induced intergranular embrittlement

Intergranular sulfur embrittlement of nickel was investigated using a dilute Ni–S alloy prepared in an inert atmosphere by arc-melting premeasured quantities of high-purity nickel and nickel sulfide at the Materials Preparation Center at Ames Laboratory. The resulting button was homogenized at 1100 °C for 1 h prior to rolling and was subsequently machined into notched impact ($16.5 \times 3.1 \times 1.5$ mm^3) and miniature tensile ($25.4 \times 5.0 \times 1.5$ mm^3) specimens. A final annealing treatment at 1100 °C for 10 min was performed to remove any damage introduced during fabrication. This procedure resulted in specimens with a mean grain size of 570 μm and a bulk sulfur concentration of 0.0024 at.% as measured by a chemical combustion analysis. To achieve even greater solute concentrations, a few specimens were sulfurized at 1000 °C for 4 h in evacuated quartz tubes with a small amount of elemental sulfur; this allowed additional sulfur to diffuse into specimens along the grain boundaries. The above-mentioned heat treatments were all terminated by water quenching to maximize the amount of sulfur trapped in the solid solution. Subsequent segregation of sulfur to the grain boundaries was controlled by heat treatments at 625 °C for times ranging from 1 to 120 h followed by air cooling. The heat treatment conditions are listed in Table 1.

Grain boundary compositions of the notched specimens, fractured at room temperature, were measured by Auger electron spectroscopy (AES) under ultrahigh vacuum (10^{-7}–10^{-8} Pa) in a Physical Electronics Model 660 Scanning Auger Microprobe. Specimens were cathodically charged with hydrogen to provide an intergranular fracture surface for analysis in a 1 N H_2SO_4

Table 1
List of heat treatment and AES analysis conditions for notched impact specimens

Heat treatments		Analysis		Relative peak intensities				Sulfur concentration, C_S (at.%)	
Sulfurization, 1000 °C (h)	Segregation, 625 °C (h)	Spots	Grains	I_{S-152}/I_{Ni-61}		I_{S-152}/I_{Ni-848}			
				Mean	S.D.	Mean	S.D.	Mean	S.D.
–	0	29	9	0.07	0.04	0.08	0.05	2.79	1.61
–	1	21	6	0.32	0.09	0.27	0.09	11.59	3.56
–	1	39	12	0.23	0.07	0.23	0.06	8.61	2.79
–	2	31	14	0.45	0.14	0.43	0.12	15.57	5.43
–	4	12	5	0.35	0.09	0.35	0.09	12.55	3.56
–	10	85	29	0.37	0.09	0.39	0.12	13.17	3.56
–	16	37	13	0.45	0.10	0.44	0.10	15.57	3.94
–	18	67	18	0.39	0.09	0.41	0.11	13.78	3.56
–	18	95	29	0.41	0.06	0.42	0.10	14.39	2.40
–	120	42	13	0.46	0.15	0.43	0.14	15.86	5.79
4	0	56	18	0.87	0.44	0.78	0.29	27.38	15.28
4	72	71	28	1.04	0.24	0.95	0.23	30.68	9.29

solution with 200 mg/l $NaAsO_2$ added as a hydrogen recombination poison. The charging was performed at room temperature for 24 h at a current density of 200 mA/cm^2, and charged specimens were stored in liquid nitrogen until testing to prevent hydrogen loss. Upon fracture, AES analysis was performed using a 3 kV electron beam with an incident current of 100 nA on focused spots with a 1.0 μm diameter. Several such spots were analyzed from the intergranular facets revealed on the fracture surface which were subsequently used to calculate arithmetically an average grain-boundary sulfur concentration and its standard deviation for each specific heat treatment. This averaging procedure allowed variations such as grain boundary structure and analysis orientation to be accounted for. The number of spot scans taken from each specimen and the number of grain boundary facets examined are given in Table 1.

The effect of grain-boundary sulfur on the mechanical properties of the nickel alloy was determined by tensile testing at a strain rate of approximately 10^{-6} s^{-1}. Tests were performed at room temperature in a flowing argon atmosphere to minimize any environmental effects. At this strain rate, the duration of the tests ranged from 4 h for the most brittle specimens to 150 h for the most ductile specimens. Ductility was determined from reduction in cross-sectional area and elongation at fracture measurements. Scanning electron microscopy (SEM) was used to characterize the fracture surfaces, and the percentage of intergranular fracture was determined using a relative area method. The maximum tensile load was measured from the engineering stress–strain curves, and the modulus of toughness was determined from the area under these curves.

2.2. Ion implantation

The critical sulfur concentration for polymorphous melting was determined by Rutherford backscattering spectrometry (RBS) of nickel specimens implanted with sulfur ions. Equal fluences of 150 keV S^+ were implanted at an average dose rate of 3.4 μA/cm^2 into two types of nickel specimens: 100 nm thick films evaporated onto MgO substrates and 3 mm thick single crystals purchased commercially. Care was taken during implantation into the single crystals to minimize channeling by aligning specimens at random orientations away from major lattice directions. All specimens were held at liquid nitrogen temperatures to minimize solute diffusion and precipitate formation. By necessity, specimens were warmed to ambient temperature for transfer between the implantation and analysis chambers. To directly measure the amount of sulfur introduced into nickel, the implantation profile was determined from RBS measurements of the evaporated films, where the film thickness and substrate material were carefully selected to provide unambiguous backscattering information from the nickel and sulfur constituents. To track the formation of the amorphous phase, the progression of dechanneling along the [1 1 0] direction in the single-crystal specimens was monitored. RBS spectra were acquired both at a [1 1 0]-aligned orientation as well as a random one; the number of counts acquired at these two orientations was monitored using the total integrated charge measured from the probing beam. All RBS spectra were collected using 1.5 MeV $^4He^+$ ions, and specimens were held at liquid nitrogen temperatures during collection to minimize noise from atomic thermal vibrations.

3. Analysis of results

3.1. Segregation-induced intergranular embrittlement

The amount of sulfur that was deposited at grain boundaries during the segregation treatments at 625 °C was determined by AES analysis of fracture surfaces from impact specimens. This analysis consistently revealed the presence of nickel and sulfur on the exposed grain boundaries of all specimens. In addition, carbon from instrumental contamination was observed to slowly appear on some specimens during analysis, which was typically completed within 3 h of fracture. No other elements were detected. For analytical purposes, all AES spectra were differentiated with respect to energy, and the resulting peak-to-peak intensities were measured. The average values of the relative intensities of the sulfur-to-nickel signals are reported in Table 1 along with the observed standard deviation among measurements. Since there are two nickel transitions that are commonly used for analysis, the intensity of the 152 eV sulfur peak is reported relative to both the 61 eV and the 848 eV nickel peaks.

The atomic sulfur concentrations are calculated from the relative peak intensities using the sensitivity factor approach [16] given by the expression

$$C_S^{GB} = \frac{I_S/S_S}{\sum_j I_j/S_j} \approx \frac{I_S/I_{Ni}}{I_S/I_{Ni} + S_S/S_{Ni}}. \quad (1)$$

Here, C_S^{GB} is the grain-boundary sulfur concentration, I_j is the peak-to-peak intensity for element j on the fracture surface, and S_j is the sensitivity factor. Since the carbon signals were consistently small when present, the general expression can be approximated using only the relative intensities of the sulfur and nickel peaks as shown. Therefore, the value of the atomic concentration depends only on the relative intensities and the relative sensitivities of the sulfur and nickel signals. The relative sensitivities of the sulfur-to-nickel signals were determined from analysis of a Ni–42 at.% S standard (std). They are given by

$$\frac{S_S}{S_{Ni}} = \frac{v_{Ni}^{std}}{v_S^{std}} \frac{I_S^{std}}{I_{Ni}^{std}}, \quad (2)$$

where v_j^{std} represents the atomic concentration of j species measured independently by chemical combustion. The sensitivities obtained from this expression for the 152 eV sulfur peak relative to the 61 and 848 eV nickel peaks are 2.44 and 3.81, respectively.

The primary difference between these two nickel signals is the sampling depth that they represent. This is reflected by the inelastic mean free path, or the escape depth, of the Auger electrons. The inelastic mean free paths, whose values depend primarily on electron energy, are 0.48, 0.51, and 1.32 nm for the 61, 152, and 848 eV signals, respectively [17]. Therefore, use of I_{S-152}/I_{Ni-61} in Eq. (1) reflects a sampling depth of 0.51 nm while use of I_{S-152}/I_{Ni-848} reflects a sampling depth of 1.32 nm. Since the maximum range of sulfur segregation is 0.5 nm on either side of a grain boundary [18–22], use of I_{S-152}/I_{Ni-61} provides a reasonable measurement of C_S^{GB}, while use of I_{S-152}/I_{Ni-848} tends to underestimate C_S^{GB}. A comparison of the calculated sulfur concentrations confirms that the values obtained using the 848 eV peak are about 66% of the values obtained using the 61 eV peak. One concern, however, in the use of the 61 eV nickel signal is that it is generally less stable than the 848 eV signal and is more susceptible to low-energy scattering. Such instability, however, was not observed in this study, and the relative values of sulfur concentrations determined from the two nickel signals (0.66) remained fairly constant among measurements, indicating the 61 eV peak was just as stable as the 848 eV peak. Because of these considerations, the sulfur concentrations listed in Table 1 are determined from I_{S-152}/I_{Ni-61}.

The distribution of sulfur on the analysis surface is shown in Fig. 3 for three non-sulfurized specimens. The histograms illustrate the range of sulfur concentrations measured over the complete set of spot scans acquired from each specimen. The three specimens shown reflect conditions where sulfur was segregated to grain boundaries at 625 °C for 0, 1, and 120 h. The histograms in the figure, which can be approximated by Gaussian distributions, have mean values and standard deviations which increase with the annealing time. These segregation kinetics are explored further in Fig. 4, which shows the effect of annealing time on C_S^{GB} using data from the complete set of notched AES specimens. The values of C_S^{GB} and the length of the error bars reflect the average values and standard deviations reported in Table 1. The data from the non-sulfurized specimens indicate that the initial C_S^{GB} is 2.79 at.% S, which increases quickly with segregation time and saturates near 15.86 at.% S. The data from the sulfurized specimens indicate that sulfurization at 1000 °C increases C_S^{GB} dramatically from 2.79 to 27.38 at.% S, yet subsequent segregation treatments at 625 °C result in only minor increases in C_S^{GB} from 27.38 to 30.68 at.% S. The kinetics of this process have been modeled using an equilibrium (Gibbsian) grain-boundary segregation analysis first presented by McLean [23] which shows how C_S^{GB} varies with the annealing time t:

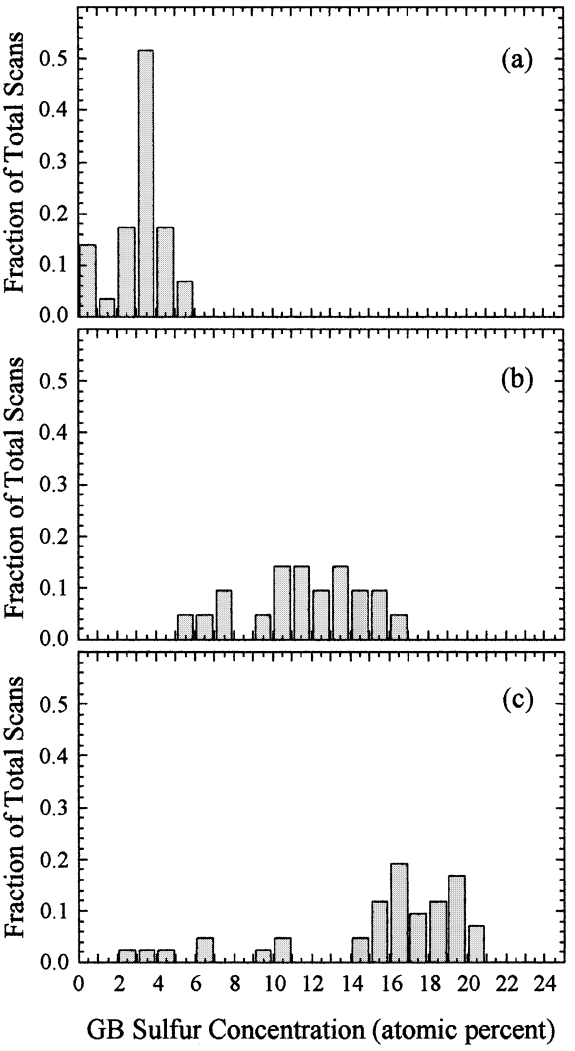

Fig. 3. Distribution of S among the intergranular facets on the fracture surfaces of three non-sulfurized specimens annealed at 625 °C for (a) 0 h, (b) 1 h, and (c) 120 h.

$$\frac{C_S^{GB}(t) - C_S^{GB}(0)}{C_S^{GB}(\infty) - C_S^{GB}(0)} = 1 - \exp\left(\frac{4Dt}{(\beta d_{GB})^2}\right) \operatorname{erfc}\left(\frac{2\sqrt{Dt}}{\beta d_{GB}}\right). \quad (3)$$

Here, D is the diffusivity, d_{GB} is the grain-boundary width, and β is the ratio of the grain-boundary concentration after infinite time to the grain interior concentration. The curves shown in Fig. 4 result from fitting the data to Eq. (3), using $D = 1.26 \times 10^{-12}$ cm^2/s (at

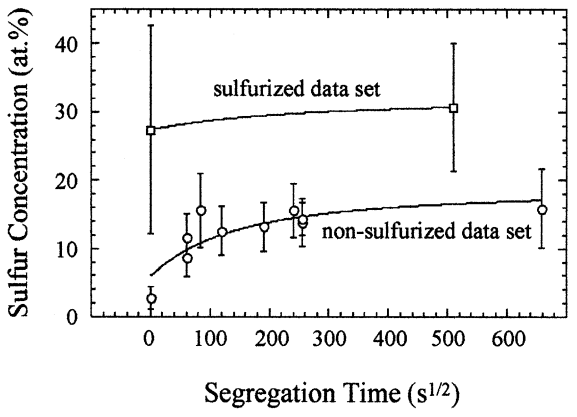

Fig. 4. Segregation kinetics of S to grain boundaries in Ni at 625 °C.

625 °C) [24] and $d_{GB} = 0.5$ nm. The values of $C_S^{GB}(0)$ and $C_S^{GB}(\infty)$ are extracted from the fit. For the non-sulfurized data, the values of $C_S^{GB}(0)$ and $C_S^{GB}(\infty)$ are 6.0 and 18.9 at.% S, respectively, and for the sulfurized data, $C_S^{GB}(0)$ and $C_S^{GB}(\infty)$ are 27.4 and 32.0 at.% S, respectively.

The results presented in Fig. 4 indicate that the sulfurization procedure successfully increases the grain-boundary sulfur concentration. However, one concern with implementing this procedure was that it could result in extensive sulfide formation either within grains or at grain boundaries. To address this issue, transmission electron microscope (TEM) specimens were prepared from sulfurized nickel to examine grain interiors for sulfide formation, and Auger depth profiles were performed to determine the depth of sulfur segregation at grain boundaries. The following results were obtained. The TEM studies revealed no detectable sulfides in the grain interiors, and the Auger depth profiles indicated a segregation depth very similar to that for non-sulfurized specimens. This depth was approximately 0.5 nm and is consistent with results reported in the literature [18–22]. Therefore, extensive sulfide formation does not appear to be an issue in these specimens.

The application of segregation treatments identical to those described above results in a clear transition from ductile to brittle behavior on tensile specimens tested at slow strain rates with increasing segregation time. This is illustrated in Fig. 5, which shows SEM images of fracture surfaces from three non-sulfurized specimens annealed at 625 °C for 0, 1, and 120 h. The AES measurements reported in Table 1 indicate that the grain-boundary sulfur concentrations corresponding to these segregation times are 2.79, 11.59, and 15.86 at.% S, respectively. As the grain-boundary sulfur concentration increases, a transition from transgranular ductile tearing to intergranular brittle fracture is evident. This trend is quantified using data from the complete set of tensile specimens, as shown in Fig. 6, where the percentage of intergranular fracture measured from the SEM images is plotted as a function of C_S^{GB}. The data indicate that the transition from transgranular to intergranular fracture occurs for values of C_S^{GB} between 10 and 16 at.% S. Similarly, this embrittlement transition is also reflected in the ductility measurements (reduction in area and elongation at fracture) and the mechanical property measurements (maximum tensile load and modulus of toughness) shown in Fig. 7. The magnitude of each of these parameters drops within this same range of C_S^{GB}, which indicates that the critical sulfur concentration to induce intergranular embrittlement lies somewhere between 10 and 16 at.% S.

3.2. Ion implantation

The thermodynamics of polymorphous melting described by the T_0 curve concept indicate that, at temperatures below T_K, implantation of S^+ ions into nickel results in the formation of an amorphous phase when the T_0 composition (~18 at.% S) is achieved. Initial studies

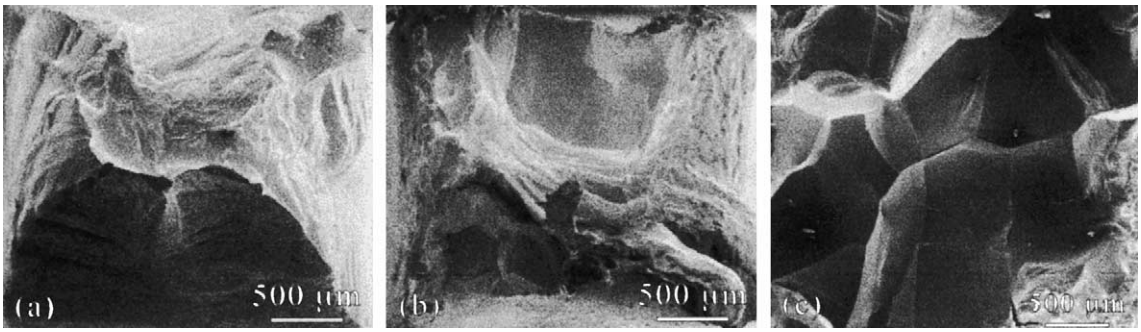

Fig. 5. Scanning electron micrographs from fracture surfaces of Ni tensile specimens which illustrate the transition from ductile transgranular to brittle intergranular fracture with increasing grain-boundary S concentrations. The average S concentrations for these specimens are (a) 2.79 at.% S, (b) 11.59 at.% S, and (c) 15.86 at.% S.

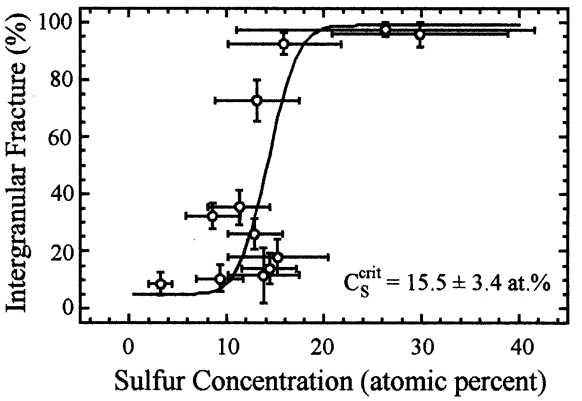

Fig. 6. Influence of grain-boundary S concentration on the transition from ductile to brittle fracture as measured by percentage intergranular fracture.

by TEM were performed to confirm the formation of this phase in a nickel specimen implanted to a dose of 6.6×10^{17} S^+/cm^2 at liquid nitrogen temperatures. The results of this examination are shown in Fig. 8, which contains a series of bright-field images and selected area diffraction patterns taken across the boundary between an amorphous region and a damaged crystalline region. The diffraction pattern from the first image indicates that diffuse intensity halos typical of the amorphous structure are present, and the subsequent images indicate that the first halo falls near the (1 1 1) reflections of the damaged nickel. Since this is the position where the first amorphous halo typically appears in fcc structures, this indicates that the amorphous phase present is from disordered nickel and not specimen contamination.

While these results confirm the formation of the amorphous phase in the nickel–sulfur system, they do not provide quantitative information on the implanted sulfur concentration or the amorphous fraction resulting from the implantation; RBS studies are used to obtain this information. The sulfur concentration, determined from a series of 100 nm thick implanted nickel films, is measured directly from RBS spectra where the energy scale of the backscattered $^4He^+$ is calibrated using gold, silicon, and nickel standards. Implantation depths are calculated from the energy difference between the leading and trailing edges measured at half maximum of the nickel signals from the relation

$$z = \frac{\Delta E}{[\varepsilon_0]n}, \tag{4}$$

where z is the depth from the surface, ΔE is the energy difference, n is the atomic density, and $[\varepsilon_0]$ is the surface energy approximation [25] for the stopping cross-section factor. Atomic concentrations, determined from the relative heights of the nickel and sulfur peaks, are calculated from the ratio of sulfur to nickel atoms, n_S/n_{Ni}, given as

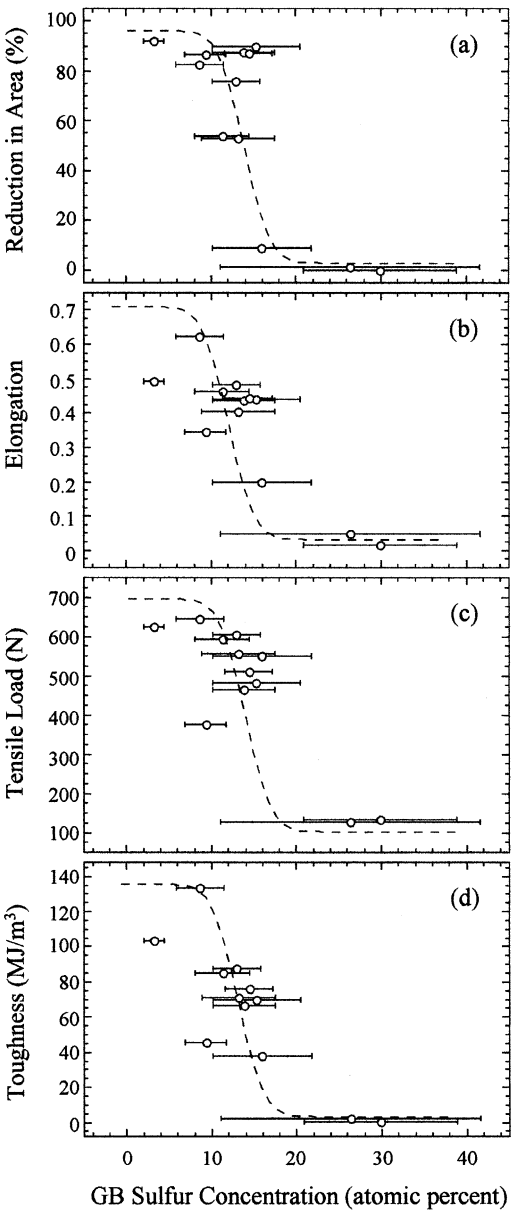

Fig. 7. Influence of grain-boundary S concentration on the transition from ductile to brittle fracture in Ni as measured by (a) reduction in area, (b) elongation at fracture, (c) maximum tensile load, and (d) modulus of toughness.

$$\frac{n_S}{n_{Ni}} = \frac{H_S}{H_{Ni}} \frac{\sigma_{Ni}(E_0)}{\sigma_S(E_0)} \frac{[\varepsilon_0]_S^{Ni}}{[\varepsilon_0]_{Ni}^{Ni}}, \tag{5}$$

where H_j is the maximum peak height, $\sigma_j(E_0)$ is the scattering cross-section at the incident beam energy E_0, and $[\varepsilon_0]_j^i$ is the stopping cross-section factor for element j

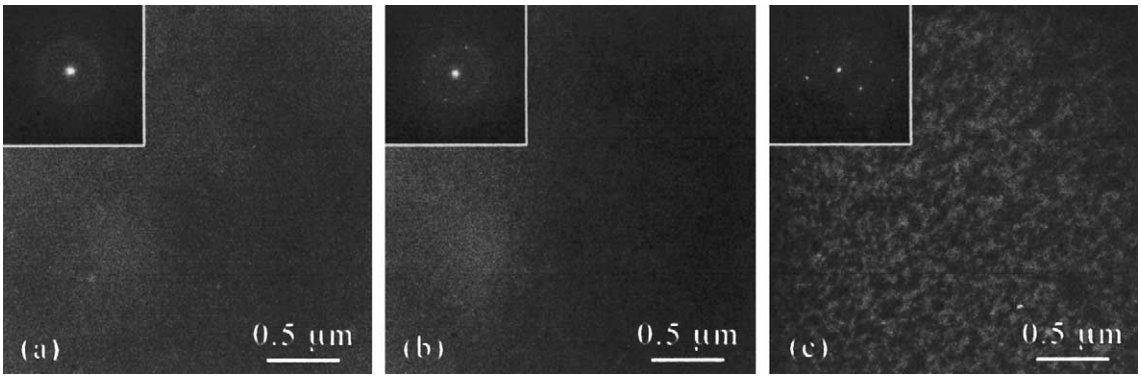

Fig. 8. Bright-field TEM micrographs and the associated selected area diffraction patterns from a backpolished Ni specimen implanted with S to a fluence of 6.6×10^{17} S^+/cm^2. The images were taken across the boundary between a completely amorphous zone and a damaged crystalline zone where (a) is primarily amorphous, (b) is partially amorphous and partially crystalline, and (c) is primarily crystalline. Such a transition is due to the increasing thickness from (a) to (b) to (c) which results in a decreasing average S concentration in the regions selected for diffraction.

in a matrix of element i. The implanted sulfur concentration, C_S^{imp}, can thus be determined from this ratio as

$$C_S^{imp} = \frac{n_S/n_{Ni}}{n_S/n_{Ni} + 1}. \quad (6)$$

Since the definitions of atomic concentration given in Eqs. (1) and (6) are self-consistent, determination of C_S^{GB} and C_S^{imp} from these expressions allows direct comparisons to be made.

The depth distributions of sulfur in the 100 nm thick nickel films are shown by the profiles in Fig. 9 for all implantation doses. The profiles, fit with Gaussian distributions, indicate a steadily increasing sulfur concentration with the implantation fluence. For fluences less than or equal to 1.0×10^{17} S^+/cm^2, the profiles have a peak range of $R_P = 70$ nm and a standard deviation of $\Delta R_P = 42$ nm; these values match well those determined by the computer simulation code TRIM [26], which predicts profiles with $R_P = 70$ nm and $\Delta R_P = 45$ nm. For fluences greater than 1.0×10^{17} S^+/cm^2, however, the profiles deviate from the prediction of the TRIM code; measured values of R_P shift toward the specimen surface due to the sputtering of nickel. This sputtering was confirmed by monitoring the decrease in thickness from the nickel signal with increasing dose; the average sputtering yield is determined to be 1.3 atoms per incident ion. The relation between dose and the implantation concentration is determined by an empirical calibration of the peak sulfur concentration, C_S^{imp} (at.%), with the implantation fluence, ϕ (S^+/cm^2); this results in the following linear expression:

$$C_S^{imp} = (9.91 \times 10^{-17})\phi + 2.23, \quad (7)$$

which is used subsequently to convert the implantation dose to sulfur concentration.

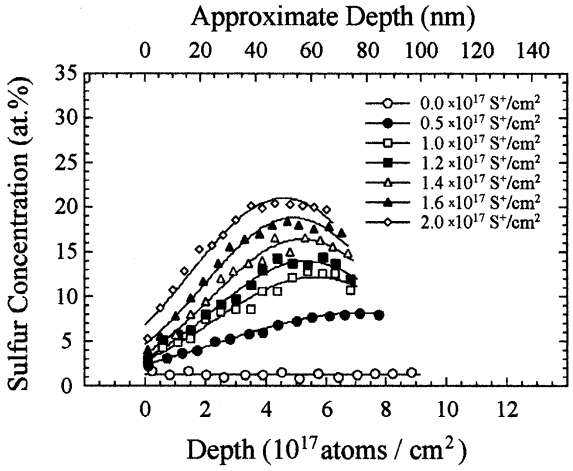

Fig. 9. RBS S profiles for several doses implanted into evaporated polycrystalline Ni film. Since the determination of the depth scale is dependent upon atomic density which also varies with depth, the depth parameter is given in terms of the product nz.

The amorphous fraction, determined from a series of 3 mm thick nickel single crystals implanted with sulfur, is measured by tracking the $^4He^+$ ion channeling along the [1 1 0] direction. The normalized channeling yield, taken as the ratio of RBS spectra acquired along the channeling direction to spectra acquired along a random non-channeling direction, is shown in Fig. 10 for each implantation dose. The formation and growth of the dechanneling peak at R_P is associated with the formation and growth of the amorphous phase observed in Fig. 8. The amorphous fraction is determined from these peaks by considering that the total normalized backscattering

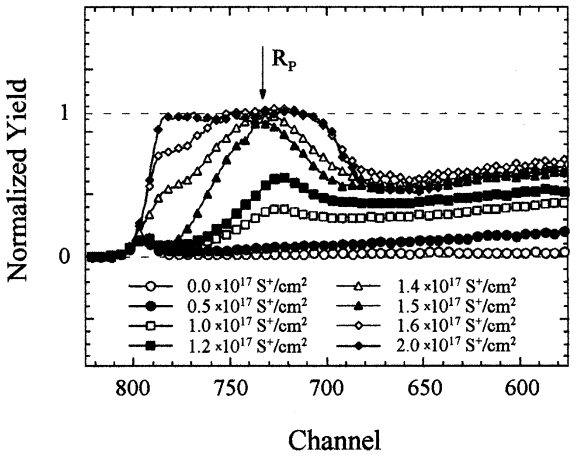

Fig. 10. RBS channeling profiles for several doses implanted into single-crystal Ni. The normalized yield increases with progressively higher doses with one exception. The normalized yield for 1.4×10^{17} S^+/cm^2 is greater than that for 1.5×10^{17} S^+/cm^2 due to the experimental error associated with measuring the implantation dose.

yield, χ_{tot}, has contributions from both the crystalline and amorphous phases [15], such that

$$\chi_{tot} = (1 - \alpha)\chi_c(\alpha) + \alpha, \tag{8}$$

where α is the amorphous fraction and χ_c is the normalized yield from the crystalline phase. Since backscattering from the crystalline phase, like that from the amorphous phase, is dependent upon α, the functional form of this dependence must be determined. This dependence of χ_c on α is estimated using the linear relation

$$\chi_c(\alpha) = \chi_c(0) + \alpha[\chi_c(1) - \chi_c(0)]. \tag{9}$$

The value of $\chi_c(0) = \chi_c(\alpha = 0)$ is taken as the backscattering background for the dose where a peak at R_P just begins to appear (0.5×10^{17} S^+/cm^2), and the value of $\chi_c(1) = \chi_c(\alpha = 1)$ is taken as the backscattering background for the dose where the peak at R_P first reaches the random level (1.4×10^{17} S^+/cm^2). The background level at R_P was determined by linear interpolation between the surface yield and the yield at $R_P + \Delta R_P$.

The effect of sulfur implantation on the amorphization of nickel is illustrated in Fig. 11. The amorphous fraction determined from Eqs. (8) and (9) is plotted as a function of the sulfur concentration determined from Eq. (7). The figure indicates that the transition from the crystalline to the amorphous state occurs over a range of sulfur concentrations between 12 and 17 at.% S. Thus, the sulfur concentration in nickel necessary for polymorphous melting at liquid nitrogen temperatures is between 12 and 17 at.% S.

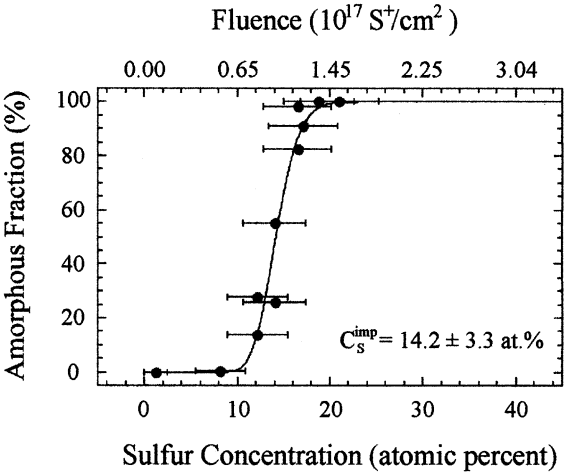

Fig. 11. Critical S concentration necessary for amorphization of Ni by S^+ ion implantation.

4. Discussion

The results of the fracture and implantation experiments in nickel indicate that the range of sulfur concentrations necessary to induce a ductile-to-brittle transition by solute segregation ($10 \leqslant C_S^{GB} \leqslant 16$ at.% S) overlaps the range of sulfur concentrations necessary to induce a crystal-to-amorphous transition by solute implantation ($12 \leqslant C_S^{imp} \leqslant 17$ at.% S). Specific values of the critical sulfur concentrations can be distilled from these ranges by applying kinetic models to these processes. Current models for implantation-induced amorphization [15] are based on the Poisson statistics of amorphous cluster formation. The chemical and structural similarities between metallic glasses and solute-segregated grain boundaries suggest that analogous models may be applied to segregation-induced intergranular fracture. Recently, such a model has been introduced for intergranular embrittlement [9] based on the Poisson statistics of polymorphous cell formation at grain boundaries.

The model for intergranular embrittlement is based on two assumptions: (1) local intergranular decohesion occurs when the sulfur concentration in elementary cells along the boundary exceeds a threshold value, and (2) the entire boundary is destabilized by an increasing number of these critical cells. This model is implemented by dividing the ideal intergranular fracture surface, the surface which would form in the case of completely brittle intergranular fracture, into elementary cells of volume $V = Ad_{GB}$, where A is the critical cell area along the grain boundary. For a given segregation treatment, the distribution of the number of sulfur atoms per cell, N, along the fracture surface is described by the Poisson probability distribution

$$P(N) = (\bar{N})^N \exp(-\bar{N})/N!, \tag{10}$$

where $\bar{N}$ represents the mean of the distribution. The validity of using Poisson statistics to model sulfur segregation to grain boundaries is illustrated in Fig. 3. Poisson statistics, which are characterized by distributions with mean values and standard deviations that increase over time, accurately portray the trends observed in the sulfur distributions with segregation time.

Since this model is based on the assumption that fracture occurs when the number of sulfur atoms in a cell reaches a critical value, N_{crit}, the percentage of intergranular fracture, %IGF, for any average sulfur concentration is given by the proportion of cells for which $N \geqslant N_{\text{crit}}$, i.e.,

$$\%\text{IGF} = \sum_{N \geqslant N_{\text{crit}}}^{\infty} P(N) \approx \frac{1}{2} + \frac{1}{2}\text{erf}\left(\frac{\bar{N} - N_{\text{crit}}}{\sqrt{2\bar{N}}}\right). \tag{11}$$

When N_{crit} is sufficiently large, the percentage of intergranular fracture can be estimated with an error function using the Gaussian approximation to the Poisson distribution as shown. This is obtained when the original summation is replaced with integration over the same range. The experimental data shown in Fig. 6 can be fit with an equation of this form; before this can be done, however, N must be related to the atomic concentration as shown by the expression

$$N = \frac{CV}{C\Omega_{\text{S}} + (1 - C)\Omega_{\text{Ni}}}, \tag{12}$$

where C is the critical solute concentration and V is the critical cell volume. The parameters Ω_S and Ω_{Ni} are the atomic volumes of sulfur and nickel calculated from tabulations of atomic radii [27]. A best fit to the data in Fig. 6 is obtained by varying the values of C and V, which influence the position of the transition and the shape of the curve, respectively. The optimum values extracted from the fit are $C = 15.5$ at.% S and $V = 0.177$ nm^3. This corresponds to a grain-boundary cell containing approximately 20 nickel atoms and 4 sulfur atoms. The model fit is shown by the curve superimposed on the data in Fig. 6.

Like the model presented above, the current kinetic models [15] for implantation-induced amorphization are also based on two assumptions. They are: (1) local amorphization occurs when the sulfur concentration in elementary clusters exceeds a threshold value, and (2) the entire region becomes amorphous by an increasing number of these critical clusters. When the peak implantation region is divided into elementary clusters of volume $V = \frac{4}{3}\pi r^3$, where r is the radius of a spherical region, the distribution of the number of sulfur ions per cluster can be described using the same Poisson probability density shown in Eq. (10). Since amorphization occurs when the number of sulfur atoms in a cluster reaches N_{crit}, the amorphous fraction is given by the same expressions for %IGF in Eqs. (11) and (12). When the data in Fig. 11 are fit with this model, the optimum values of $C = 14.2 \pm 3.3$ at.% S and $V = 2.360$ nm^3 are extracted. This corresponds to a spherical cluster containing roughly 220 nickel atoms and 47 sulfur atoms with a radius of $r = 0.77$ nm. The curve which best fits the experimental data is plotted in Fig. 11.

A comparison of the critical concentrations derived from these two models indicates that the critical concentration of 15.5 ± 3.4 at.% S necessary to cause intergranular fracture is well within experimental error of the 14.2 ± 3.3 at.% S required to induce the crystal-to-amorphous transformation. This is of fundamental significance for understanding fracture in this system because it implies that segregation-induced intergranular fracture, like ion-implantation-induced amorphization, is a result of disorder-induced melting, albeit one localized to regions at grain boundaries. The localized nature of this disorder-induced intergranular fracture is reflected in a comparison of the cell and cluster volumes extracted from the fitting procedures. The optimum cell volume for intergranular fracture (0.177 nm^3) is significantly less than the optimum cluster volume for implantation-induced amorphization (2.360 nm^3). While the latter volume represents a spherical cluster with a diameter of 1.54 nm, the former represents a cell of thickness $d_{\text{GB}} = 0.5$ nm and area $A = 0.354$ nm^2; this can also be approximated as a cubic cell with a side of 0.57 nm or a sphere of diameter 0.70 nm. Regardless of the shape, however, this cell volume is small enough to exist within the typical segregation zone at a grain boundary [18–22]. Thus, the cell volume extracted from the optimum fit to the experimental data using the kinetic model for intergranular embrittlement accurately reflects the physical interaction volume at grain boundaries. It should be noted, however, that the scatter in the experimental data in Fig. 6 allows for a number of fits that fall within the acceptable error range yet are not optimized to the data; this has the implication that different cell volumes may be obtained by using non-optimized fits.

While both the critical concentrations for intergranular fracture and implantation-induced amorphization fall within experimental error of each other, they both fall short of the 18 at.% sulfur estimated from the polymorphous melting curve. There are two possible explanations for this difference. The first is based on the fact that the T_0 curve in Fig. 2 is only an estimation. It was determined by calculating the midpoint concentration between the liquidus and solidus curves. Since data for these curves only exist at temperatures above the eutectic, extrapolation below the eutectic temperature was necessary to determine the T_0 concentrations at low temperatures, and this extrapolation could slightly skew the results. The second explanation for the difference is based on the thermodynamics of disorder-induced

melting. As illustrated in Fig. 1, the thermodynamics implies that any process or condition that raises the free energy of a defective crystal can contribute to melting. The analyses presented up to this point have only considered the free-energy increase caused by misfit sulfur atoms in nickel. While this is the primary source of stable atomic disorder in this system, other secondary sources are also present. For example, inherent grain-boundary disorder, elastic strain, dislocations, and irradiation-induced defects are all potential sources of static atomic disorder which may serve to raise the free energy of the defective crystal. If these additional sources raise the free energy sufficiently, this would result in an underestimate of the critical sulfur concentration for disorder-induced melting.

While the above considerations take into account primary and secondary sources of atomic disorder which raise the free energy of solute-segregated grain boundaries, they do not directly consider the role of stress in the fracture process. Stress can be an indirect source of atomic disorder in that it can generate dislocations and elastic strain. More importantly, however, the applied stress provides a physical mechanism for the separation of specimens embrittled by grain-boundary sulfur segregation. This is necessary since segregation-induced embrittlement is not expected to occur simultaneously on all grain boundaries. Rather, the amount of sulfur differs among grain boundaries due to the relative orientation between grains, as illustrated by the distributions in Fig. 3. The impact of this variation is that only grain boundaries with sulfur concentrations greater than the critical value (15.5 ± 3.4 at.%) will be susceptible to disorder-induced melting. While stress may provide the additional disorder necessary to raise the free energy of the remaining grain boundaries, the experimental results presented here cannot verify this. The results, however, can illustrate the role of stress in the fracture process. In specimens identified as primarily brittle, the SEM micrographs in Fig. 5 still reveal regions of ductile tearing on transgranular fracture surfaces; in addition, these specimens can still have elongations up to 20%, as illustrated in Fig. 7(c). These observations indicate that stress is necessary to physically separate regions where grain-boundary sulfur concentrations are below the critical value.

The synergistic effects of sulfur and hydrogen co-segregation on intergranular fracture can be explained by the accumulation of static atomic disorder. While the secondary sources of disorder listed above only have a small effect on the critical sulfur concentration for polymorphous melting in nickel, the presence of hydrogen solute at grain boundaries has a much more significant effect. This is illustrated in the data from the straining electrode tests performed by Bruemmer et al. [5] on dilute nickel–sulfur alloys, which show that the critical C_S^{GB} for intergranular fracture drops dramatically as hydrogen solute is cathodically charged into specimens. These data are plotted in Fig. 12 for charging potentials of -0.72, -0.56, -0.43, and -0.30 V measured relative to a saturated calomel reference electrode (SCE). In addition, the results of the tensile tests performed in this study are also included in the figure; since these tests were performed in the absence of charging, the corresponding potential is taken as $+0.24$ V (SCE), which is equivalent to 0.00 V relative to a standard hydrogen reference electrode. To properly compare the experimental results of the two studies, all values of C_S^{GB} have been recalculated from the I_{S-152}/I_{Ni-848} relative peak intensities since these are the only values reported for the straining electrode experiments. Even though this results in an underestimate of the sulfur concentration due to sampling depth considerations, comparisons of the relative trends in the data can still be made. Data taken at each charging potential have been fit using the statistical model for intergranular fracture presented in Eq. (11).

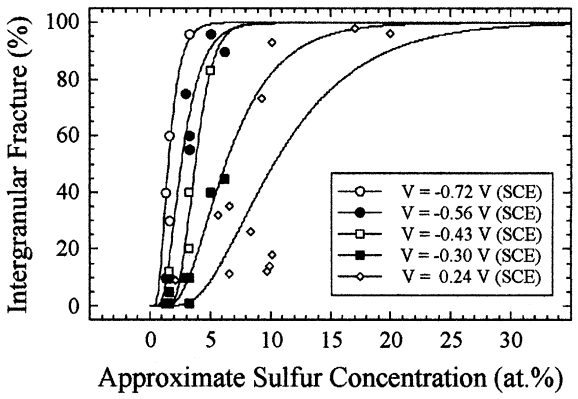

Fig. 12. The effect of cathodic charging potential on the determination of the critical S concentration for intergranular fracture. The 0.24 V (SCE) data come from this study, and the additional data are taken from the straining electrode tests by Bruemmer et al. [5].

The fits shown in Fig. 12 illustrate the decrease in the critical sulfur concentration with an increasingly cathodic hydrogen charging potential. This dependence is more clearly shown in Fig. 13 where the values of C_S^{GB} extracted from the kinetic model for intergranular fracture are plotted against the cathodic potential. The data indicate that a first-order linear approximation provides a reasonable fit. Since the charging potential is an indirect measure of the grain-boundary hydrogen concentration, C_H^{GB}, the data also reflect the relation between the critical C_S^{GB} and the critical C_H^{GB} necessary to induce intergranular fracture. While the dependence between C_S^{GB} and the cathodic potential is roughly linear, the dependence between C_S^{GB} and C_H^{GB} is not clear because the relation between the hydrogen potential and

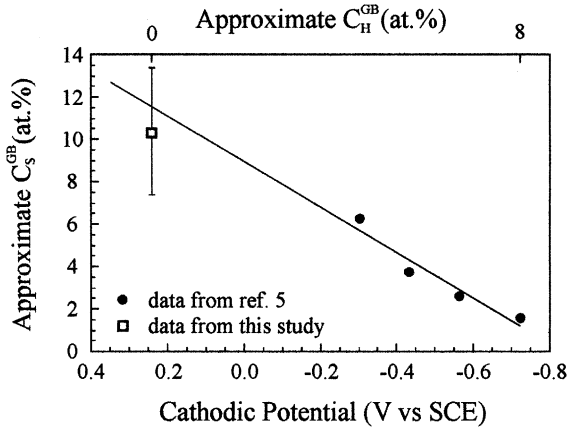

Fig. 13. The synergistic effects of S and H co-segregation on intergranular fracture.

C_H^{GB} is not known. However, while C_H^{GB} cannot be determined for all of the data in the figure, it can be estimated for two cases. Hydrogen embrittlement studies of nickel based on a diffusion analysis [28,29] indicate that $C_H^{GB} \sim 8$ at.% H when sulfur is not present at grain boundaries ($C_S^{GB} = 0$ at.% S). Similarly, the sulfur embrittlement studies performed here based on experimental measurement indicate that $C_S^{GB} \sim 16$ at.% S when hydrogen is not present at grain boundaries ($C_H^{GB} = 0$ at.% H). Therefore, the correlation between the charging potential and C_H^{GB} is shown on the upper abscissa in Fig. 13 for these two points. While this reveals the range of hydrogen concentrations that influences intergranular embrittlement, it does not reveal the functional form of the dependence.

The synergistic effects of sulfur and hydrogen co-segregation on intergranular fracture can be described in terms of polymorphous melting by extending the T_0 curve concept into three dimensions. This is illustrated in Fig. 14(a), where a polymorphous melting surface is shown in the three-dimensional space defined by the C_S, C_H, and T axes. It is constructed from the lines of intersection on the three primary planes; these are determined from the Ni–S T_0 curve in Fig. 2 for the T–C_S plane, the Ni–H T_0 curve for the T–C_H plane, and the curve in Fig. 13 for the C_S–C_H plane. In addition, the experimental data from Fig. 13 are superimposed on the polymorphous melting surface in a plane parallel to the C_S–C_H plane at the appropriate experimental temperature (298 K). Unlike the fit in Fig. 13, the line that runs through these data is generalized as a gentle curve since the functional form between C_S and C_H is not known. The region that lies within the volume defined by this surface and the three main planes is one of crystal stability. The regions that lie outside of this volume, on the other hand, are ones where the crystal state is unstable relative to the liquid or glass; at temperatures above T_K,

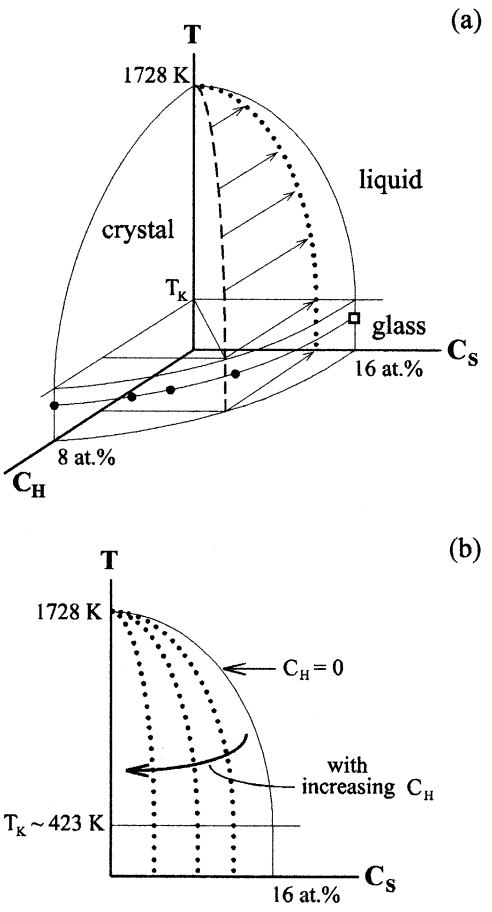

Fig. 14. (a) A semi-quantitative polymorphous melting surface for intergranular fracture in Ni based on the interactions of S and H at grain boundaries. (b) A projection of the polymorphous melting surface onto the T–C_S plane illustrating how the addition of H decreases the critical S concentration for polymorphous melting in Ni.

this instability is relative to the supercooled liquid, and at temperatures below T_K, this instability is relative to the glass. The effect of hydrogen on the critical sulfur concentration for intergranular fracture is illustrated by the dashed line that falls along the polymorphous melting surface. Projection of this line onto the T–C_S plane is shown as the dotted line in the figure. Projection of similar lines that fall along the polymorphous melting surface results in a series of Ni–S T_0 curves shown in Fig. 14(b), which indicate progressively lower critical sulfur concentrations for polymorphous melting with increasing hydrogen. Projection of the same curves onto the T–C_H plane results in a similar series of Ni–H T_0 curves that predict progressively lower hydrogen concentrations for polymorphous melting with increasing sulfur.

5. Conclusion

In conclusion, studies of the effect of sulfur segregation to grain boundaries on the fracture of nickel indicate that a critical concentration of 15.5 ± 3.4 at.% S exists for intergranular embrittlement. In addition, studies of sulfur implantation into nickel reveal that a similar critical concentration of 14.2 ± 3.3 at.% S exists to drive the crystal-to-amorphous transformation. A comparison of these values indicates that they are equivalent within experimental error. Since implantation-induced amorphization is a disorder-induced melting process driven by the accumulation of static atomic disorder from misfitting solute atoms, it is suggested that the same is true for solute-induced intergranular embrittlement, albeit it is one restricted to localized grain interfaces. The localized nature of this melting is suggested by the small calculated interaction volume for intergranular fracture (0.177 nm^3) in comparison to the large calculated interaction volume for implantation-induced amorphization (2.360 nm^3). These values were extracted from optimum fits to the experimental data using kinetic models based on Poisson statistics. Finally, the synergistic interaction of sulfur and hydrogen solutes on intergranular fracture in nickel was examined by introducing a semi-quantitative polymorphous melting surface.

Acknowledgements

This work was supported by the US Department of Energy, Office of Science, under contract W-31-109-Eng-38. Ion implantation and backscattering experiments were performed at the HVEM Tandem Accelerator Facility at Argonne National Laboratory with extensive help from P.M. Baldo, L.L. Funk, and A.W. McCormick. Slow-strain-rate tensile tests were performed using the Stress Corrosion Cracking facilities at Argonne National Laboratory with the assistance of H.M. Chung, D.R. Perkins, and W.E. Ruther. Auger electron spectroscopy was performed at the Center for Microanalysis of Materials at the University of Illinois with guidance from N. Finnegan. Special thanks are extended to B.J. Kestel for aid with specimen preparation.

References

[1] W.C. Johnson, J.E. Doherty, B.H. Kear, A.F. Giamei, Scr. Metall. 8 (1974) 971.
[2] S.M. Bruemmer, R.H. Jones, M.T. Thomas, D.R. Baer, Scr. Metall. 14 (1980) 1233.
[3] C. Loier, J.-Y. Boos, Metall. Trans. A 12 (1981) 1223.
[4] R.H. Jones, S.M. Bruemmer, M.T. Thomas, D.R. Baer, Metall. Trans. A 14 (1983) 1729.
[5] S.M. Bruemmer, R.H. Jones, M.T. Thomas, D.R. Baer, Metall. Trans. A 14 (1983) 223.
[6] R.P. Messmer, C.L. Briant, Acta Metall. 30 (1982) 457.
[7] M.E. Eberhart, K.H. Johnson, R.M. Latanision, Acta Metall. 32 (1984) 955.
[8] D.H. Lassila, H.K. Birnbaum, Acta Metall. 35 (1987) 1815.
[9] J.K. Heuer, P.R. Okamoto, N.Q. Lam, J.F. Stubbins, Appl. Phys. Lett. 76 (2000) 3403.
[10] M.F. Ashby, F. Spaepen, S. Williams, Acta Metall. 26 (1978) 1647.
[11] D.E. Polk, Scr. Metall. 4 (1970) 117.
[12] P.R. Okamoto, N.Q. Lam, L.E. Rehn, Solid State Phys. 52 (1999) 1.
[13] P.R. Okamoto, J.K. Heuer, N.Q. Lam, S. Ohnuki, Y. Matsukawa, K. Tozawa, J.F. Stubbins, Appl. Phys. Lett. 73 (1998) 473.
[14] W. Kauzmann, Chem. Rev. 43 (1948) 219.
[15] C. Cohen, A. Benyagoub, H. Bernas, J. Chaumont, L. Thomé, M. Berti, A.V. Drigo, Phys. Rev. B 31 (1985) 5.
[16] K.D. Childs, B.A. Carlson, L.A. LaVanier, J.F. Moulder, D.F. Paul, W.F. Stickle, D.G. Watson, Handbook of Auger Electron Spectroscopy, 3rd Ed., Physical Electronics, Eden Prairie, MN, 1995.
[17] S. Tanuma, C.J. Powell, D.R. Penn, Surf. Interface Anal. 17 (1991) 911.
[18] H.L. Marcus, L.H. Hackett, Jr., P.W. Palmberg, in: Temper Embrittlement of Alloy Steels, ASTM STP 499, American Society for Testing and Materials, 1972, p. 90.
[19] P.R. Howell, D.E. Fleet, T.F. Page, B. Ralph, in: Proceedings of the 3rd International Conference on Strength of Metals and Alloys, vol. 1, 1973, p. 149 (Paper 30).
[20] D.A. Smith, G.D.W. Smith, in: Proceedings of the 3rd International Conference on Strength of Metals and Alloys, vol. 1, 1973, p. 144.
[21] P.R. Howell, D.E. Fleet, A. Hildon, B. Ralph, J. Microsc. 107 (1976) 155.
[22] R.W. Balluffi, in: W.C. Johnson, J.M. Blakely (Eds.), Interfacial Segregation, American Society of Metals, Metals Park, PA, 1977.
[23] D. McLean, Grain Boundaries in Metals, Clarendon, Oxford, 1957.
[24] S.J. Wang, H.J. Grabke, Z. Metallkd. 61 (1970) 597.
[25] W.-K. Chu, J.W. Mayer, M.-A. Nicolet, Backscattering Spectrometry, Academic Press, New York, 1978.
[26] J.P. Biersack, L.G. Haggmark, Nucl. Instrum. Meth. 174 (1980) 257.
[27] W.L. Masterson, E.J. Slowinski, C.L. Stanitski, Chemical Principles, 6th Ed., Saunders College, Philadelphia, PA, 1985.
[28] D.H. Lassila, H.K. Birnbaum, Acta Metall. 36 (1988) 2821.
[29] J. Yao, S.A. Meguid, J.R. Cahoon, Metall. Trans. A 24 (1993) 105.